



# Recent progress in the development of KBe<sub>2</sub>BO<sub>3</sub>F<sub>2</sub>: a deep-UV nonlinear optical crystal

Lijuan Liu<sup>1</sup> · Lin Zhao<sup>2</sup> · Xingjiang Zhou<sup>2</sup> · Xiaoyang Wang<sup>1</sup>

Received: 30 September 2021 / Accepted: 20 December 2021 / Published online: 8 January 2022  
© The Author(s), under exclusive licence to Springer-Verlag GmbH Germany, part of Springer Nature 2022

## Abstract

This review mainly introduces in detail the progress of KBBF crystal over the last decade, with a full description of its crystal growth, new phase in hydrothermal growth, revised Sellmeier equations of the refractive index, improved prism-coupled devices, and the related new deep-UV laser sources. Several important applications on angle-resolved photoemission spectroscopy will be reviewed. Finally, we give a prospect about the future development of KBBF crystals.

## 1 Introduction

All-solid-state deep-ultraviolet (deep-UV) coherent light sources ( $\lambda < 200$  nm) have many important applications in the frontiers of science and technology, such as photolithography, precise micro-machining, and angle-resolved photoemission spectroscopy (ARPES) [1, 2]. An effective approach is to use commercially available, visible or near-infrared all-solid-state lasers as the fundamental frequency light source to generate deep-UV laser line through cascaded frequency conversion by nonlinear optical (NLO) crystals [3]. We define the deep-UV NLO crystal that can output deep-UV lasers by direct second harmonic generation (SHG). As is well known, borates have played an important role in the NLO materials since the discovery of  $\beta$ -BaB<sub>2</sub>O<sub>4</sub> (BBO) by Chen et al. in the 1980s [4]. Chen developed the anionic group theory in 1976–1978, which clarified the internal relationship between microstructure and NLO effects [5–8]. This theory is systematically summarized in Ref. [9], which provides a simple criterion of structure selection for the discovery of new NLO crystals. Based on the

systematic study, Chen's team has discovered a series of excellent NLO crystals represented by  $\beta$ -BaB<sub>2</sub>O<sub>4</sub> (BBO), LiB<sub>3</sub>O<sub>5</sub> (LBO) [10] and KBe<sub>2</sub>BO<sub>3</sub>F<sub>2</sub> (KBBF) [11]. The history of KBBF has been introduced in a review by Chen et al. in 2009 [3], including its discovery, crystal growth, structure, basic optical properties and applications.

This review can be regarded as a sequel to Ref. [3]. In this review, we will focus on the progress of KBBF and its related deep-UV lasers generation in the last ten years. In the second section, we review the exploration of deep-UV NLO crystals in the post-KBBF era; in the next section, we introduce the crystal growth of KBBF by both flux and hydrothermal methods. In the section on optical properties of KBBF, its device fabrication and revised Sellmeier equations are discussed. In the fifth section, we describe the deep-UV lasers generation based on KBBF prism-coupled device (PCD). In the last section, we present the important applications of deep-UV lasers in ARPES. Finally, some perspectives are provided on the future development of KBBF crystals.

## 2 Exploration of deep-UV NLO crystals in the post-KBBF era

The shortest SHG wavelength of a NLO crystal is determined by the combined effect of the UV absorption edge and the birefringence of a crystal. Because there is serious dispersion near the UV absorption edge, even a large birefringence of the crystal may not guarantee the phase-matching (PM) condition at short wavelength for SHG. So, a short UV absorption edge is desired for deep-UV NLO

✉ Xiaoyang Wang  
xywang@mail.ipc.ac.cn

<sup>1</sup> Key Laboratory of Functional Crystals and Laser Technology, Beijing Center for Crystal Research and Development, Technical Institute of Physics and Chemistry, Chinese Academy of Sciences, Beijing 100190, People's Republic of China

<sup>2</sup> Beijing National Laboratory for Condensed Matter Physics, Institute of Physics, Chinese Academy of Sciences, Beijing 100190, People's Republic of China

crystals. The shorter the UV absorption edge, the better the crystal. In addition, a larger birefringence is also desired for deep-UV crystals. As can be seen from Table 1, the two typical examples are BBO and LBO crystals, which are two kinds of NLO crystals that have been commercialized. BBO has the largest birefringence in borates ( $\Delta n=0.12$  at 1064 nm), its UV absorption edge is 189 nm, however its shortest SHG wavelength can only reach 205 nm due to the limitation of phase-matching; while the UV absorption edge of LBO crystal is 150 nm, but the birefringence is so small ( $\Delta n=0.04$  at 1064 nm) that the shortest SHG wavelength can only reach 278 nm. CLBO crystal has proven to be an intermediate example. Its UV absorption edge is similar to BBO, though its birefringence is less than half of it, and its shortest frequency doubling wavelength can only reach 238 nm. CLBO is almost the only NLO crystal that can realize high power output of 266 nm laser (fourth harmonic generation of Nd-based laser) and is gradually becoming commercialized. As a contrast, KBBF and its family compound RbBe<sub>2</sub>BO<sub>3</sub>F<sub>2</sub> (RBBF) [12] (K replaced by Rb) have a short UV absorption edge (~150 nm) and moderate birefringence ( $\Delta n=0.08/0.075$  at 1064 nm), so their shortest SHG wavelengths are 161 and 170 nm, respectively. They are veritable deep-UV NLO crystals, i.e., the shortest SHG wavelength is below 200 nm, while the other crystals are not.

In fact, sum-frequency technology can also be used to generate deep-UV laser lines that are shorter in wavelength than the shortest SHG wavelength attainable for a NLO crystal. However, it is technically complex because the two input lasers with different wavelengths need to meet strict conditions including time synchronization, spatial superposition, and polarization matching in the sum-frequency process. These make it more challenging for the sum-frequency technology especially in the deep-UV region.

As mentioned above, deep-UV NLO crystals must first meet the PM conditions, and then some other conditions,

such as large second-order NLO coefficient, good physical and chemical properties, and easy growth and processing for applications. So far, only KBBF and RBBF have been proved to be deep-UV NLO crystals by experiments [12, 14]. The comprehensive performance of KBBF is better than that of RBBF. The superiority is increasingly obvious as the wavelength becomes shorter. KBBF is a benchmark for deep-UV crystals. It was once reported by the journal *Nature* with a title of “China’s crystal cache” [15]. Since then, exploring and discovering new deep-UV NLO crystals have become a hot research topic. Researchers first focused their attention on the compounds similar to the KBBF family, and found a series of new NLO crystals, such as SBBO family ( $\text{Sr}_2\text{Be}_2\text{B}_2\text{O}_7$ ,  $\text{Ba}_2\text{Be}_2\text{B}_2\text{O}_7$ ) [16, 17], NaCaBe<sub>2</sub>B<sub>2</sub>O<sub>6</sub>F [18], NaSr<sub>3</sub>Be<sub>3</sub>B<sub>3</sub>O<sub>9</sub>F<sub>4</sub> [19] and NBBO family ( $\text{NaBeB}_3\text{O}_6$ ,  $\alpha\text{-KBe}_2\text{B}_3\text{O}_7$ ,  $\beta\text{-KBe}_2\text{B}_3\text{O}_7$ ,  $\gamma\text{-KBe}_2\text{B}_3\text{O}_7$ ) [20]. Unfortunately, the existing evidence cannot prove that their NLO performance is better than that of KBBF. Therefore, Chen et al. pointed out in 2014 that “KBBF almost achieves the theoretical limits of deep-UV NLO borates, and it would be a great challenge to discover other borates which have comparable NLO capability, especially for coherent light production below the wavelength of 190 nm by direct SHG” [21].

There is no end to scientific exploration. In recent years, the so-called “fluorooxoborate” (also known as “fluorinated borate”) has attracted people’s attention, which originated from the discovery of three kinds of lithium fluorooxoborate  $\text{LiB}_6\text{O}_9\text{F}$  [22],  $\text{Li}_2\text{B}_3\text{O}_4\text{F}_3$  [23] and  $\text{Li}_2\text{B}_6\text{O}_9\text{F}_2$  [24] by German scientists. In general, fluorine atoms in fluorooxoborates are directly connected to metal atoms, and the basic anionic groups are  $[\text{BO}_3]$  and  $[\text{BO}_4]$ . As its name implies, fluorooxoborate is characterized by the fact that fluorine atoms are connected to boron atoms directly instead of oxygen atoms to form  $[\text{BO}_3\text{F}]$  or  $[\text{BO}_2\text{F}_2]$  groups. Recently, a series of fluorooxoborates, such as  $\text{MB}_4\text{O}_6\text{F}$  ( $\text{M}=\text{NH}_4$ , Cs, Rb, Na) [25–28],  $\text{MB}_5\text{O}_7\text{F}_3$  ( $\text{M}=\text{Ca}$ , Sr) [29, 30] and  $\text{M}_2\text{B}_{10}\text{O}_{14}\text{F}_6$

**Table 1** Properties of common nonlinear optical crystals

Crystal	Point group	Transmittance (nm)	Birefringence $\Delta n$ at 1064 nm	SHG coefficients $d_{ij}$ (pm/V)	Shortest SHG wavelength (nm)
KTP	mm2	350–4500	0.089	$d_{31}=1.4$	500
LBO	mm2	150–2600	0.04	$d_{32}=1.04$ $d_{33}=0.06$	278
CBO	222	166–3400	0.053	$d_{14}=1.15$	273
CLBO	$\bar{4}2m$	180–2750	0.05	$d_{36}=0.95$	238
KABO	32	180–3780	0.068	$d_{11}=0.48$	225
BBO	3m	189–3300	0.12	$d_{22}=1.6$ $d_{31}=0.96$	205
RBBF [12]	32	151–3500	0.075	$d_{11}=0.45$	170
KBBF	32	147–3660	0.080	$d_{11}=0.49$	161

The data come from references [13] except RBBF

(M=Ca, Sr) [31], have been discovered successively, which are declared to be potential deep-UV NLO crystals.

Fluoroxyborate can only be synthesized and grown into crystals in an anhydrous and oxygen-free environment. So, the whole process must be carried out in a sealed environment, which is unfavorable for its crystal growth. To our knowledge, no large-sized fluoroxyborate crystal has been reported up to date. As a result, their linear and NLO properties like the transmittance, birefringence and NLO coefficients are still studied on the theoretical stage. It is conjectured that even if a large crystal can form under a certain favorable condition, it will not be stable in the ambient environment.

In addition, two new KBBF analog crystals have been found including NH<sub>4</sub>Be<sub>2</sub>B<sub>2</sub>O<sub>7</sub> (ABBF) and  $\gamma$ -Be<sub>2</sub>BO<sub>3</sub>F (BBF) [32]. Theoretical calculations show that  $\gamma$ -BBF may be the best deep-UV NLO crystal, with UV absorption edge down to about 145 nm and shortest SHG wavelength at 146 nm.  $\gamma$ -BBF crystal melts incongruently and can be grown by the hydrothermal method, but it is a great challenge to grow large-sized crystals. It is worth mentioning that BBF has three phases ( $\alpha$ -BBF [33],  $\beta$ -BBF [34],  $\gamma$ -BBF), which brings extra difficulty to crystal growth. Crystals available for properties testing have not been obtained yet. Some of the above-mentioned crystals with potential deep-UV NLO properties in the post-KBBF era are summarized in Table 2 and compared with KBBF.

### 3 Progress in crystals growth

#### 3.1 Flux method

The growth of KBBF crystal has its own particularity. Due to the use of highly toxic beryllium compounds in the process of synthesis and growth, it is harmful to human body and environment. Therefore, operators should wear masks, and the whole operation process must be carried out in a sealed system, using a sealed glove box, a closed growth furnace in a ventilation cupboard. While the whole cupboard is in a state of weak negative pressure, the gas is continuously

pumped into the filter water tank for 24 h, then discharged into the atmosphere after two stages of filtration which is conformed to the relevant national regulations. This not only brings great inconvenience to crystal growth, but also increases the cost of crystal growth.

The second special feature is that KBBF has a strong-layered habit, which is difficult to grow thick along the Z-axis direction, and the crystal is flaky with a thickness of < 1 mm. In terms of mechanical properties, the cleavage of the crystal along the *a*-*b* plane is so serious that it is difficult to obliquely cut into devices along the PM angle.

The third special feature is that KBBF crystals cannot grow with a seed (the reason is estimated to relate to its serious layered structure), so it can only be grown by a spontaneous nucleation method [36], which brings great difficulties to the growth of large-size and high-quality crystals.

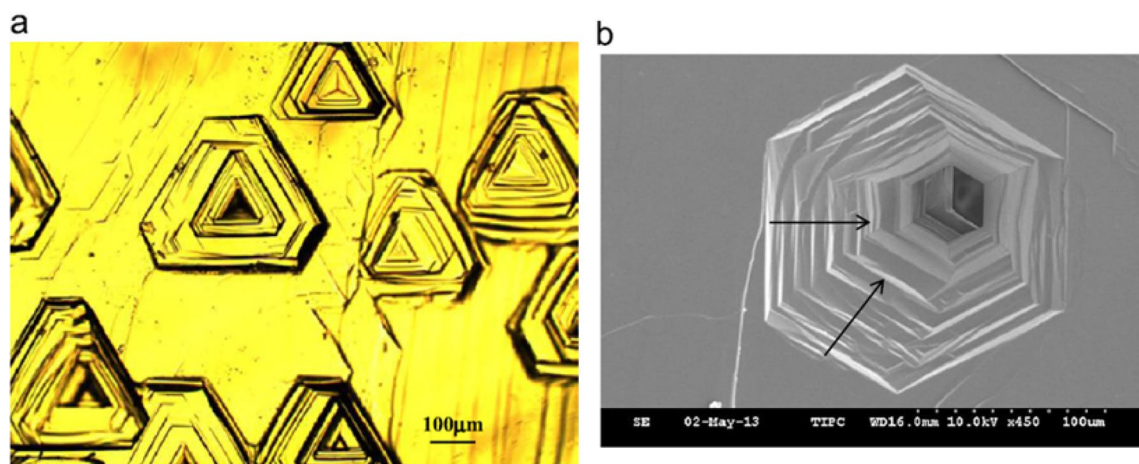
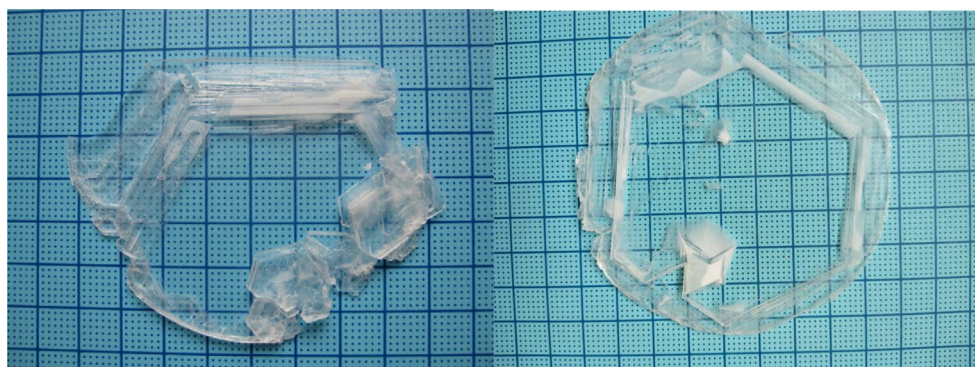
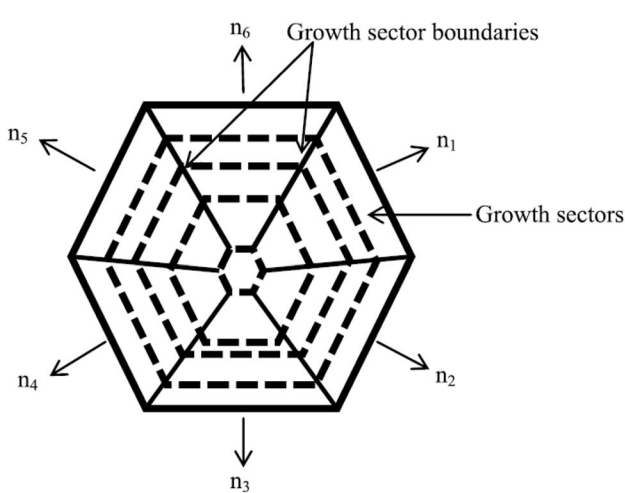
KBBF incongruently melts, so it can be grown by both the flux and hydrothermal method [37, 38]. In the last ten years, crystal growth has made continuous breakthroughs. A “localized spontaneous nucleation method” is developed, which controls the initial spontaneous nucleation to a single one and limits the second spontaneous nucleation [36]. A special temperature gradient in the furnace along both the horizontal and vertical directions is developed so that a single nucleus could be grown at the center of the crucible and continues to grow large. We have also developed a “temperature oscillation method” to eliminate unexpected small nucleus [36]. The obtained KBBF crystal is close to a large single one. The main body has a hexagonal shape which reflects the symmetry of the crystal, only some small crystals grown by secondary nucleation are adhered to the edge (Fig. 1). The maximum thickness of obtained KBBF crystals (Z-axis direction) can reach 4.0 mm.

The defects of KBBF crystals were also studied. The major defects observed include stripes, inclusions, dislocations and twin boundaries. By chemical etching in HF solution, regular triangle etching pits were observed by both optical microscope and SEM (Fig. 2). The 2D schematic of KBBF is shown in Fig. 3, which indicates that the crystal is grown from a small nucleus in the center and continues to grow large along the sixth directions as denoted as  $n_i$  [39].

**Table 2** NLO properties of the new potential crystals in the post-KBBF era

Crystal	Space group	UV absorption edge (nm)	Birefringence ( $\Delta n$ at 1064 nm)	SHG effect	Theoretical shortest SHG wavelength (nm)
KBBF	R32	147	0.080	$d_{11}=0.49$ pm/V	161
CsB <sub>4</sub> O <sub>6</sub> F [26]	Pna2 <sub>1</sub>	155	0.114	1.9 ( $\times$ KDP)	172 <sup>a</sup>
NH <sub>4</sub> B <sub>4</sub> O <sub>6</sub> F	Pna2 <sub>1</sub>	156	0.117	3.0 ( $\times$ KDP)	164 <sup>a</sup> [25]/158 <sup>a</sup> [35]
ABBF [32]	R32	153		1.2 ( $\times$ KDP)	174
$\gamma$ -BBF [32]	R32	144.8		2.3 ( $\times$ KDP)	146 <sup>a</sup>

<sup>a</sup>Theoretical results

**Fig. 1** As-grown KBBF crystals**Fig. 2** **a** Etching pits on the (001) face observed by the optical microscope. **b** An etching pit on the (001) face observed by SEM (the black arrow indicates the etching direction)**Fig. 3** The schematic of crystal morphology, the crystal was divided into six sectors.  $n_i$ =growth directions, contours of the crystal at different stages of growth

### 3.2 Hydrothermal method

KBBF crystal growth by the hydrothermal method was first reported by Ye and Tang [37]. In our studies, we started to grow KBBF by the hydrothermal method in 2009 cooperating with the Guilin Research Institute of Geology for Mineral Resources [40]. Transparent KBBF crystals were obtained as shown in Fig. 4. The maximum thickness could reach to 9.0 mm, as shown in Fig. 5. Unfortunately, we first reported that the NLO effect of the hydrothermal-grown KBBF are rather poor with varied SHG intensities for different samples, and its SHG conversion efficiency is one or two orders of magnitude smaller than that of the flux-grown ones [3]. The reason was investigated and it was discovered that there are three unidentified small peaks in the powder X-ray diffraction pattern observed in the hydrothermal-grown KBBF crystals [41]. The extra peaks are indexed to be (113), (119) and (11 15) by a new structure of  $R\bar{3}c$ . The new structure with cell parameters of  $a=4.422(1)$  Å and  $c=37.524(3)$  Å was determined by powder X-ray diffraction and Rietveld refinement for the first time (Fig. 6).

**Fig. 4** Hydrothermally grown KBBF crystals

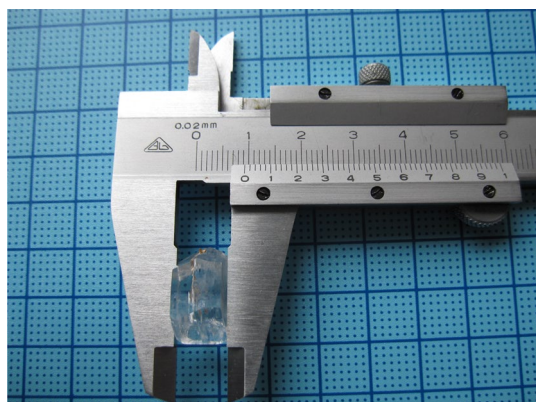
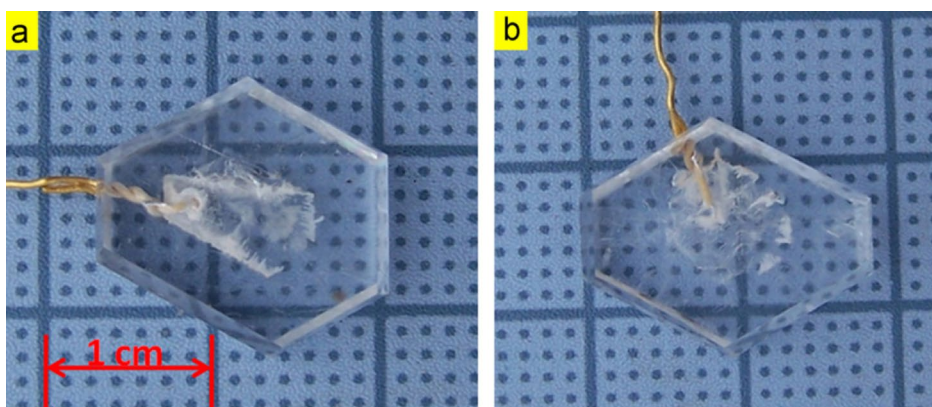


**Fig. 5** Hydrothermally grown KBBF crystal thickness along the Z-axis

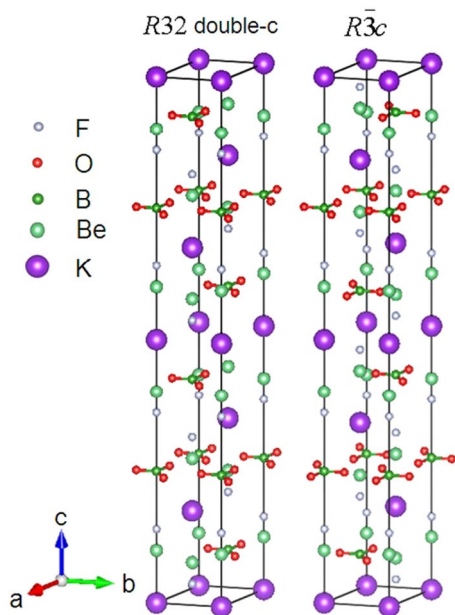


**Fig. 6** KBBF crystal structure (left: by flux method; right: by hydrothermal method)

The new structure is centrosymmetric and therefore has no SHG effect. Compared to the R32 structure of flux-grown KBBF [3], the R̄3c structure has the same anionic groups of  $(\text{BO}_3)^{3-}$  triangles and  $(\text{BeO}_3\text{F})^{5-}$  tetrahedral as fundamental building units. However, the arrangement of the planar  $(\text{BO}_3)^{3-}$  groups between adjacent  $(\text{Be}_2\text{BO}_3\text{F}_2)_n$  layers are slightly different. As illustrated in Fig. 6, there are six  $(\text{Be}_2\text{BO}_3\text{F}_2)_n$  layers in each R̄3c unit cell and each layer has one  $(\text{BO}_3)^{3-}$  group. Among them, three layers of  $(\text{BO}_3)^{3-}$  groups have the same direction and the other three layers of them are in the opposite direction (rotated 60° along the Z-axis) which counteracts the SHG effect completely. More complicated, the hydrothermal-grown KBBF crystals are supposed to be microscopic intergrowth of both R32 and R̄3c structures. The composition between the R32 and R̄3c phases determines the SHG intensity, which is consistent with various SHG intensities for different samples [3]. After that, Sang et al. proved the R̄3c structure in the hydrothermal-grown KBBF by both single crystal diffraction and neutron diffraction methods [42]. Finally, we have successfully observed two kinds of electron diffraction patterns in the hydrothermal-grown KBBF by TEM that also confirms the coexistence of two structures [43].

Up till now, it is still a great challenge to grow KBBF with R32 single phase by the hydrothermal method. At present, all the effective output of deep-UV laser is based on flux-grown KBBF crystals.

#### 4 Revised Sellmeier equations

The first accurate refractive index data of KBBF crystal were obtained in 2008 [44]. At that time, only seven light sources in the visible region could be used to measure refractive index data. The Sellmeier equations have been obtained within an accuracy of four significant figures derived from the refractive index data combined with the PM characteristics in the deep-UV region. However, Nakazato et al.

reported that the refractive index equation is not accurate enough for sum-frequency generation (SFG) in the deep-UV region, for example, the calculated PM angles according to the Sellmeier equations in Ref. [44] for 5 HG of Ti:sapphire laser in the 149.8–160 nm range were 3–4 degrees smaller than the observed ones. Such large differences are not acceptable and it will affect the precision manufacture of KBBF devices [45]. So it is necessary to further modify the Sellmeier equations of KBBF to obtain accurate PM angle for SFG in the deep-UV region. The refractive index data of KBBF were measured again by a SpectroMaster UV–VIS–IR apparatus (Trioptics, Hamburg, Germany). Unlike before [44], the light source has been expanded from near IR to deep-UV region, in which there are nine monochromatic lights from UV to near IR, i.e., Hg lamp emissions at 0.253, 0.363, 0.404, 0.435 and 0.546 μm, Cd lamp at 0.480 and 0.643 μm, He lamp at 0.587 μm and Cs lamp at 0.852 μm, respectively. The light sources in the deep-UV range were obtained by frequency quadrupling through two successive SHG steps of LBO and KBBF crystals from a Ti:sapphire laser (Coherent Chameleon Ultra II, 80 MHz, and 140 fs). The new refractive index data were shown in Table 3 [46]. Li et al. proposed a new dispersion relation based on assuming double resonances of polarizabilities of KBBF in the deep-UV region which can fit to the measured refractive indices and agree with the observed PM angles for SFG. A revised Sellmeier equations with six parameters have been derived as (wavelength unit: μm):

$$n_0^2 = 1.024248 + \frac{0.9502782 \cdot \lambda^2}{\lambda^2 - 0.0738546^2} + \frac{0.1960298 \cdot \lambda^2}{\lambda^2 - 0.1298386^2} - 0.0113908 \cdot \lambda^2 \quad (1)$$

$$n_0^2 = 0.9411543 + \frac{0.8684699 \cdot \lambda^2}{\lambda^2 - 0.0646955^2} + \frac{0.1256642 \cdot \lambda^2}{\lambda^2 - 0.1196215^2} - 0.0044736 \cdot \lambda^2. \quad (2)$$

The new dispersion relations not only fit the measured refractive indices accurately but also agree with the PM angle measurement in the deep-UV region down to 165 nm. The present work will help to design new KBBF devices applied in the deep-UV region.

## 5 Deep-UV lasers generation based on KBBF-PCD

### 5.1 KBBF prism-coupled technology

Since KBBF is grown as a thin plate along the *a*–*b* plane and easily cleaves along the *Z*-axis, it is difficult to cut the crystal along the PM direction. To solve this problem, Chen and Xu developed a special KBBF prism-coupled device

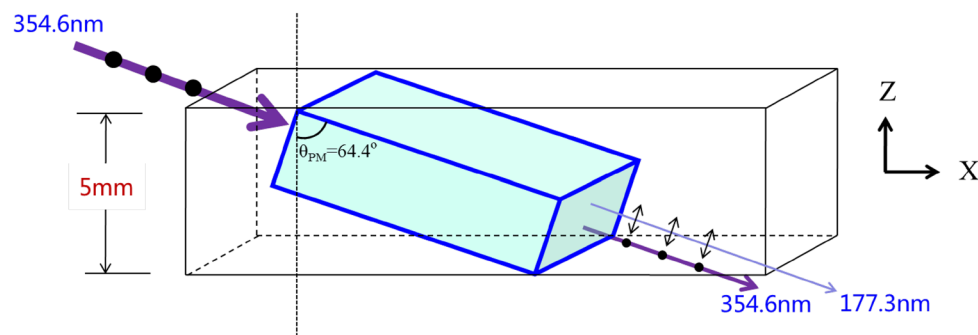
**Table 3** Measured and calculated refractive indices of KBBF crystal

$\Lambda$ (μm)	$n_0$		$n_e$	
	Exp	Cal	Exp	Cal
0.1870	1.59005(3)	1.59004	1.4629(2)	1.46296
0.1900	1.58444(1)	1.58462	1.45991(2)	1.45998
0.1930	1.57995(2)	1.57963	1.45738(2)	1.45721
0.2000	1.56922(3)	1.56938	1.45132(6)	1.45141
0.2537	1.525622(2)	1.52559	1.425262(1)	1.42526
0.3650	1.496001(1)	1.49600	1.406414(1)	1.40641
0.4047	1.491298(1)	1.49129	1.403363(1)	1.40334
0.4358	1.488494(1)	1.48848	1.401530(1)	1.40152
0.4800	1.485387(1)	1.48542	1.399513(1)	1.39952
0.5461	1.482080(1)	1.48210	1.397370(1)	1.39737
0.5876	1.480484(2)	1.48052	1.39633(3)	1.39637
0.6438	1.47875(6)	1.47879	1.39524(7)	1.39527
0.7065	1.47727(2)	1.47723	1.39430(5)	1.39431
0.8521	1.47456(3)	1.47449	1.39274(1)	1.39269
1.014	1.47213(4)	1.47213	1.39142(6)	1.39141
1.530	1.46544(3)	1.46546	1.38821(3)	1.38822

(KBBF-PCD) in 2001 [47]. Usually the KBBF crystal is sandwiched between two  $\text{SiO}_2$  or  $\text{CaF}_2$  prisms by optical contact so that the fundamental frequency laser can propagate along the PM direction in KBBF. With this technique, sixth harmonic generation from a picosecond pulsed Nd:YVO<sub>4</sub> laser at 177.3 nm was successfully generated for the first time in 2003 [48]. The second generation of

“deep-bonding” KBBF-PCD was developed in 2014 [49]. The surfaces of both KBBF and prisms were polished and coated with  $\text{SiO}_2$  films via electron beam evaporation using a deep-UV coating machine (Leybold Optics SYRUSpro 1110), then KBBF and the prisms were optically contacted and slowly heated to 120 °C for 2 days to allow  $\text{SiO}_2$  molecules to bond tightly between two surfaces. The “deep-bonding” technique can efficiently eliminate impurities or bubbles between the interfaces and is beneficial to improve the laser damage threshold of the PCD to a certain extent. However, the damage threshold of PCD is two orders of magnitude lower than that of KBBF crystals itself, which limits the output power of deep-UV lasers. Furthermore, the lower transmittance of PCD due to the two extra interfaces limits the output power of cw deep-UV lasers.

**Fig. 7** A prism-free frequency doubling device of KBBF crystal



The long-term goal in future is to fabricate prism-free frequency doubling devices (normal doubler) of KBBF crystals (Fig. 7), that is, the device is cut along the phase-matching direction. It is known from Fig. 7 that the thickness along the Z-axis of the KBBF crystal must reach at least 5 mm to ensure that a device of  $2 \times 2 \times 6$  mm<sup>3</sup> can be cut. The challenge originates from the difficulty of growing thick KBBF crystals and the inclination of cleavage during cutting.

## 5.2 High power of 6th harmonic generation at 177.3 nm

In the last ten years from 2010 to 2020, the goal toward deep-UV lasers was higher output power, shorter wavelength, and continuous-wave (cw) generation. Using a deep-bonding KBBF-PCD, a maximum output power of 200 mW and a stable average of 72.2 mW at 177.3 nm were obtained for the first time [50]. In this experiment, the fundamental laser source was a Nd:YAG laser at 1064 nm with a high repetition rate of 1 MHz, 10 ps and a beam quality factor  $M^2 < 1.3$ . Two LBO crystals were fabricated for the first SHG and second Type-II THG to produce 354.7 nm. The surfaces of both KBBF (1.58 mm thick) and CaF<sub>2</sub> prisms were optically polished and coated with SiO<sub>2</sub> films as shown in Fig. 8a to form a prism-coupled device. A copper water-cooled holder was designed to maintain the KBBF-PCD temperature as shown in Fig. 7b. The output power and conversion efficiency at 177.3 nm dependent on the input power at 355 nm are shown in Figs. 9 and 10, respectively. The average power was measured under an input power of 7.6 W over 30 min, as shown in Fig. 11. In future, W-level 177.3 nm deep-UV laser is expected and will depend on prism-free frequency doubling devices of KBBF crystals.

## 5.3 Shorter-wavelength generation in the VUV region

In 2011, Nomura et al. have obtained a quasi-cw laser in the vacuum-UV (VUV) region at 153 nm at 33 MHz repetition rate by SFG [51]. It is achieved by successive frequency conversions from an Yb-doped fiber laser centered

at 1074 nm using two LBO crystals and two KBBF-PCDs. The final output at 153 nm is generated by a SFG process  $\omega(o) + 6\omega(o) \rightarrow 7\omega(e)$  in a KBBF-PCD with a maximum power of 1 nW. Though the power of 1 nW is rather low, it is enough for certain precision spectroscopy experiments. In 2016, Nakazato et al. simplified the experimental process using a SFG process  $\omega(o) + 4\omega(o) \rightarrow 5\omega(e)$  with one LBO crystal and two KBBF-PCD in a 6 kHz Ti:sapphire laser system. The experimental setup is shown in Fig. 12. They have successfully obtained 3.6  $\mu$ W at 149.8 nm and 110  $\mu$ W at 154.0 nm, respectively, which is the shortest wavelength ever obtained by PM method in nonlinear optical crystals [45]. The dependence of  $5\omega$  output power on the wavelength is shown in Fig. 13. The thicknesses of KBBF crystals are 2.3 mm for the fourth harmonic generation and 0.86 mm for the fifth harmonic generation because it is close to the UV absorption edge where there is strong absorption.

In 2015, a 167.75 nm VUV laser was generated by eighth harmonic generation (EHG) of a mode-locked 1342 nm Nd:YVO<sub>4</sub> laser through two LBO crystals and

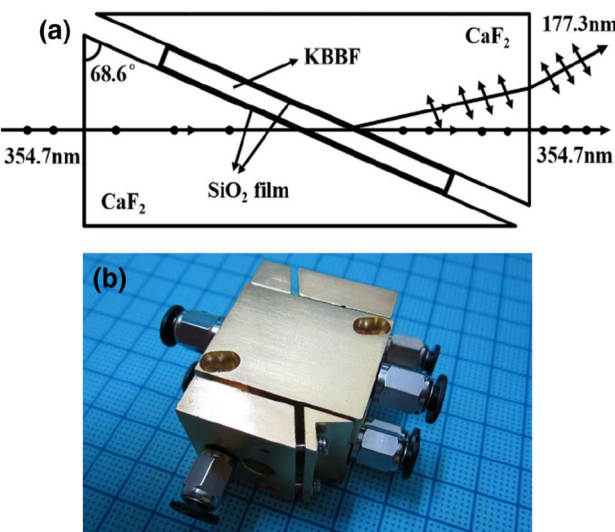


**Fig. 8** **a** Schematic of the diffusion-bonded KBBF-PCD, **b** the copper water-cooled holder of KBBF-PCD. ([Reprinted/Adapted] with permission from Xu et al. [50] © The Optical Society)

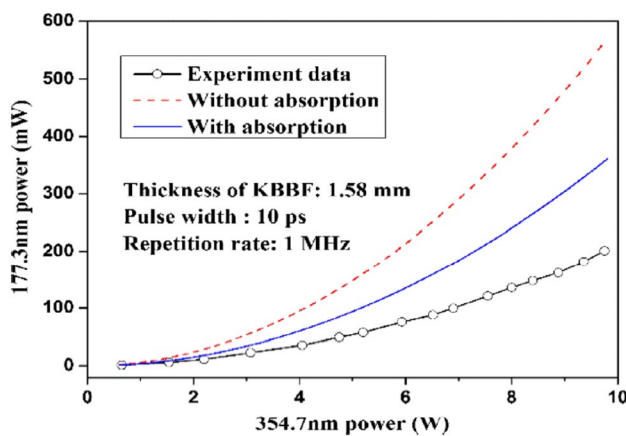


**Fig. 9** The 177.3 nm output power versus the 355 nm input power. The solid line is the quadratic fit. ([Reprinted/Adapted] with permission from Xu et al. [50] © The Optical Society)

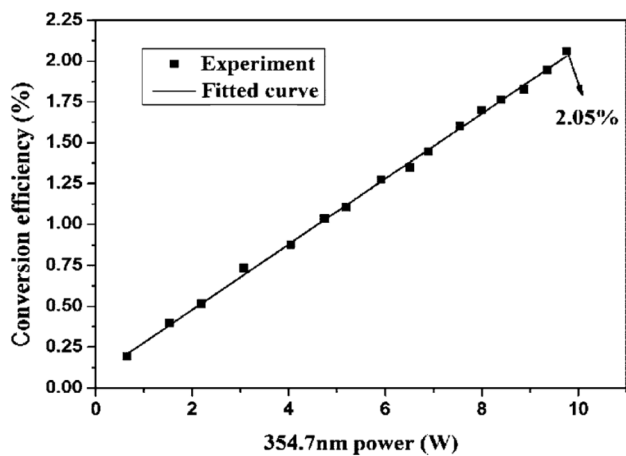


**Fig. 10** The conversion efficiency versus the 355 nm input power. ([Reprinted/Adapted] with permission from Xu et al. [50] © The Optical Society)

one KBBF-PCD [52]. In the experiment, the fundamental Nd:YVO<sub>4</sub> laser system is 17 W at 77 MHz repetition rate and 24 ps pulse duration. A maximum average output power of 65 μW at 167.75 nm was obtained with an input power of 0.63 W at 335.5 nm. In 2018, Li et al. reported a high-energy single-frequency deep-UV solid-state laser at 167.079 nm by the EHG of a diode-pumped Nd:LGGS laser [53]. A KBBF-PCD with a KBBF (16×6×1.22 mm<sup>3</sup>) sandwiched between a front quartz crystal and a real trapezoid CaF<sub>2</sub> prism was used in this experiment (Fig. 14). The experimental setup is shown in Fig. 15. Figure 16 shows the dependence of 8ω deep-UV pulse energy on 4ω UV input energy. A maximum deep-UV laser output energy of 1.5 μJ is achieved with the input UV power of 20 mJ at a repetition rate of 5 Hz and 200 μs pulse duration. This deep-UV source is useful for the

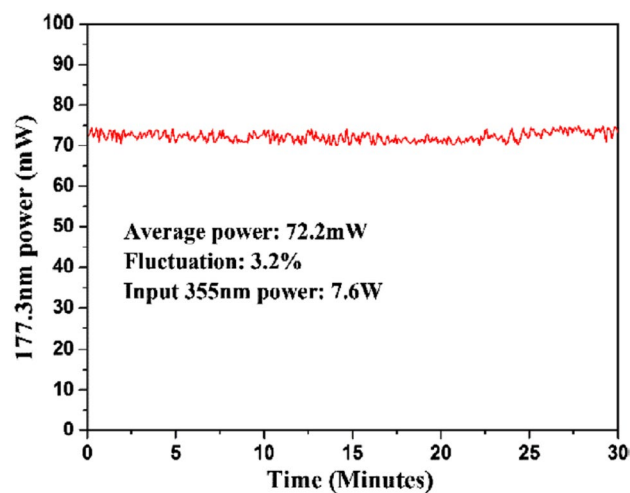


**Fig. 11** Stability of the 177.3 nm output power at 72.2 mW over 30 min. ([Reprinted/Adapted] with permission from Xu et al. [50] © The Optical Society)

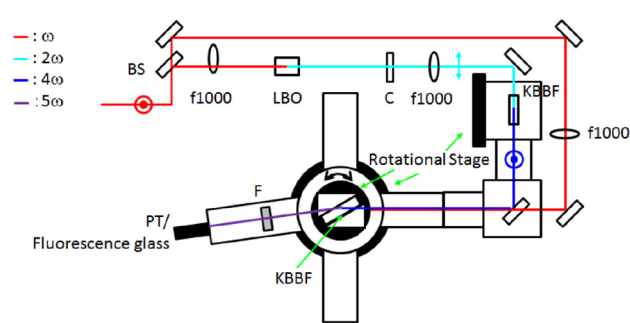


**Fig. 12** Schematic diagram of frequency conversion system. BS beam splitter (R90%, T10%), C chopper (12.5% of duty), PT phototube, F filter. ([Reprinted/Adapted] with permission from Nakazato et al. [45] © The Optical Society)

direct detection of a <sup>27</sup>Al ion via resonance fluorescence in a multi-ion optical clock.

Based on the EHG of a nanosecond pulsed 1319 nm Nd:YAG laser, a 2.14 mW deep-UV laser at 165 nm was achieved with a repetition rate of 1 kHz [54]. The generated radiation at 165 nm is the shortest deep-UV wavelength ever generated through direct SHG method and the highest average power of all-solid-state lasers below 170 nm to our knowledge. The experimental setup is shown in Fig. 17. The dependence of the output power at 165 nm on the pump power at 330 nm was measured as shown in Fig. 18.

#### 5.4 Continuous-wave deep-UV laser generation

Continuous-wave (cw) ultraviolet lasers have wide applications range from wafer inspection in the semiconductor

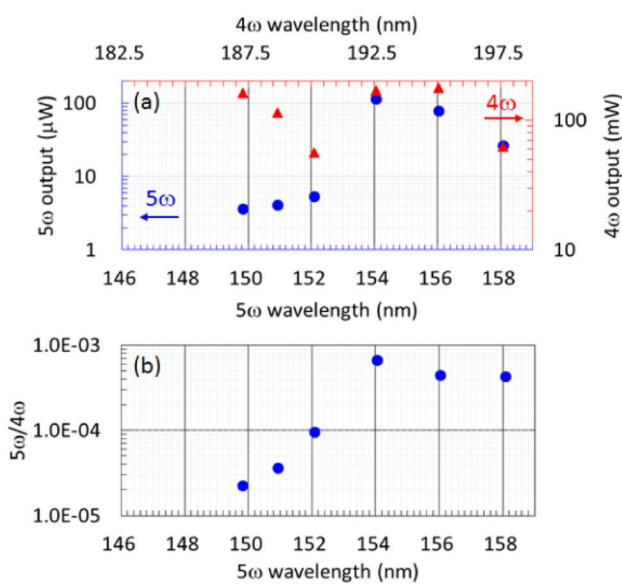


**Fig. 13** **a** The dependence of  $5\omega$  output power on  $5\omega$  wavelength. The  $4\omega$  input powers for generating  $5\omega$  are also shown along with  $4\omega$  wavelength. **b** The ratio of the  $5\omega$  output power to the  $4\omega$  input power depending on  $5\omega$  wavelength. ([Reprinted/Adapted] with permission from Nakazato et al. [45] © The Optical Society)

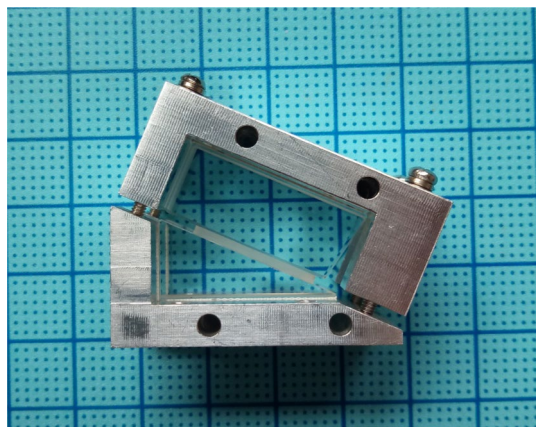


**Fig. 14** KBBF-PCD for 167 nm generation

industry to photoemission spectroscopy as a basic research method. In 2012, the first cw laser generated with KBBF-PCD by a SHG process was taken from 382 to 191 nm [55]. To avoid the Fresnel reflection at the surface, a Brewster-cut prism was prepared for the fundamental wavelength with an apex angle of  $55.8^\circ$  (Fig. 19). The initial wavelength of 764 nm was converted to 382 nm in a commercially available TA-SHG pro by Toptica Photonics. A maximum output power of 700 mW at 382 nm was generated with an estimated linewidth  $< 70$  kHz. The second frequency conversion

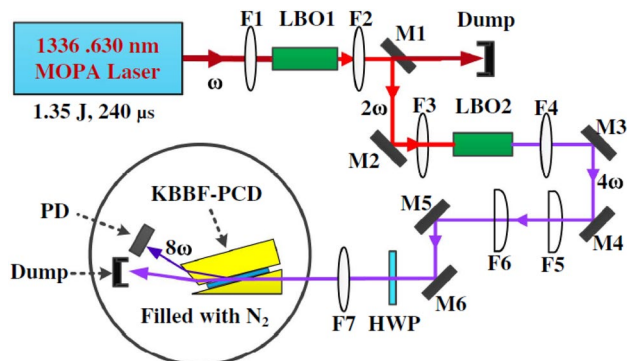


**Fig. 15** Experimental setup for 167.079 nm generation. ([Reprinted/Adapted] with permission from Li et al. [53] © The Optical Society)

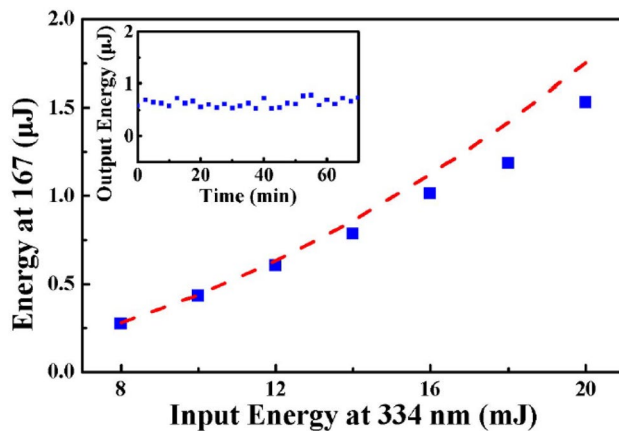


**Fig. 16** DUV output energy at  $\sim 167$  nm versus incident energy at 334 nm. The blue squares represent the experimental data; the red dashed line shows the simulation results. Inset: energy stability of a DUV laser at an average output energy of 0.6  $\mu$ J over 1 h. ([Reprinted/Adapted] with permission from Li et al. [53] © The Optical Society)

was also realized in a cavity in a bow-tie configuration with the Brewster-cut KBBF-PCD in it. A maximum output power of 1.3 mW at 191 nm was generated from the Brewster-cut KBBF-PCD (Fig. 20a). Figure 20b depicts a stable measurement of the TA, the 382 nm and the 191 nm over an interval of 8 h. No degradation of the 191 nm power level was observed.

For applications in metrology and lithography or the seeding of excimer lasers, deep-UV laser powers at 10–100 mW are expected. In 2013, over 15 mW cw laser emission at 193 nm was generated using KBBF-PCD, which can meet the demand in metrological applications [56]. The experimental setup is shown in Fig. 21. The dependence of the deep-UV output power on the fundamental power at 386 nm was shown in Fig. 22. With a maximum power of 1.65 W

**Fig. 17** Experimental setup for generating ns DUV laser at 165 nm. ([Reprinted/Adapted] with permission from Dai et al. [54] © The Optical Society)

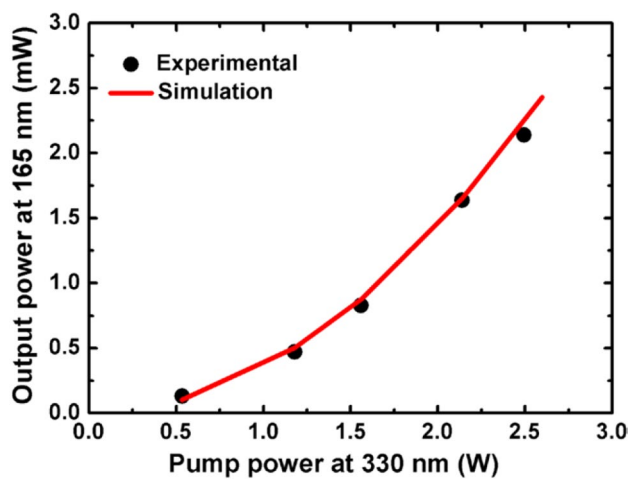
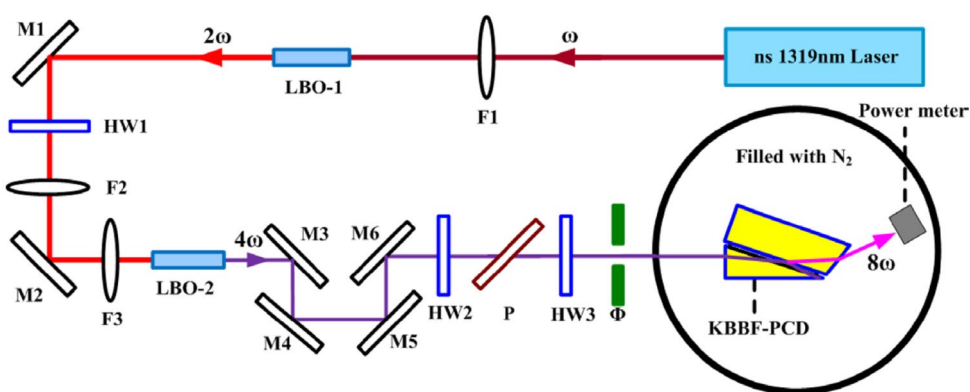


**Fig. 18** DUV output power at 165 nm versus UV pump power at 330 nm for KBBF effective length of 2.7 mm. Black spots represent the experimental data; the results of simulation are shown by the red line. ([Reprinted/Adapted] with permission from Dai et al. [54] © The Optical Society)

at 386 nm, over 15 mW of output power at 193 nm was obtained. Moreover, the stability test was also measured over 80 h and no degradation of the deep-UV power was observed (Fig. 23).

As the wavelength becomes shorter, the refractive index difference between the KBBF and the prism ( $\text{CaF}_2$  or fused quartz) becomes larger. The Fresnel reflection at the interfaces between the prism and KBBF crystal increases. For example, the Fresnel reflection at one interface between  $\text{CaF}_2$  and KBBF crystal is 0.37% for a 382 nm → 191 nm laser, and 1.25% for 354.6 nm → 177.3 nm, respectively. That is to say, the maximum transmittance of the PCD can only reach 99.26% and 97.5%, respectively, where a minimum transmittance of ~99% for the device is usually required to frequency double a cw laser. In addition, the scattering at the interfaces becomes increasingly larger as the wavelength becomes shorter. The overall transmittance will be further reduced. In this case, it is challenging to generate cw lasers with a wavelength shorter than 191 nm using PCDs.

## 6 Applications of the deep-UV lasers on ARPES

Based on the KBBF-PCD, deep-UV laser with a photon energy 6.994 eV can be generated. The utilization of this deep-UV coherent laser as a light source for photoemission spectroscopy possesses many obvious advantages in several major aspects, such as super-high-energy resolution, super-high photon flux, and enhanced bulk sensitivity, when compared with traditional light sources like synchrotron radiation and discharge lamps [57]. It has enabled photoemission spectroscopy achieve a sub-meV energy resolution and provides an efficient, compact and low-cost light source for the laboratory-based photoemission spectroscopy systems. Based on this deep-UV laser, various types of vacuum ultraviolet (VUV) photoemission spectroscopies have been developed [58], including VUV laser-based ARPES with

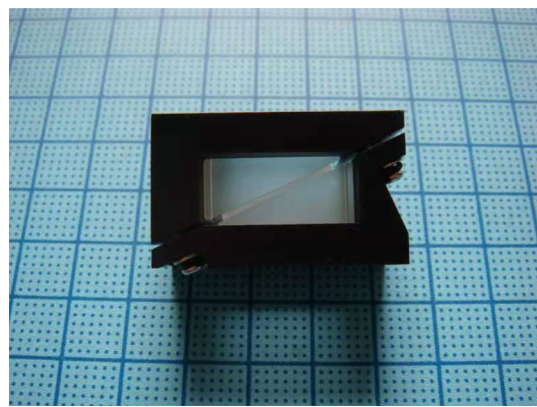


**Fig. 19** A Brewster-cut KBBF-PCD for 191 nm generation

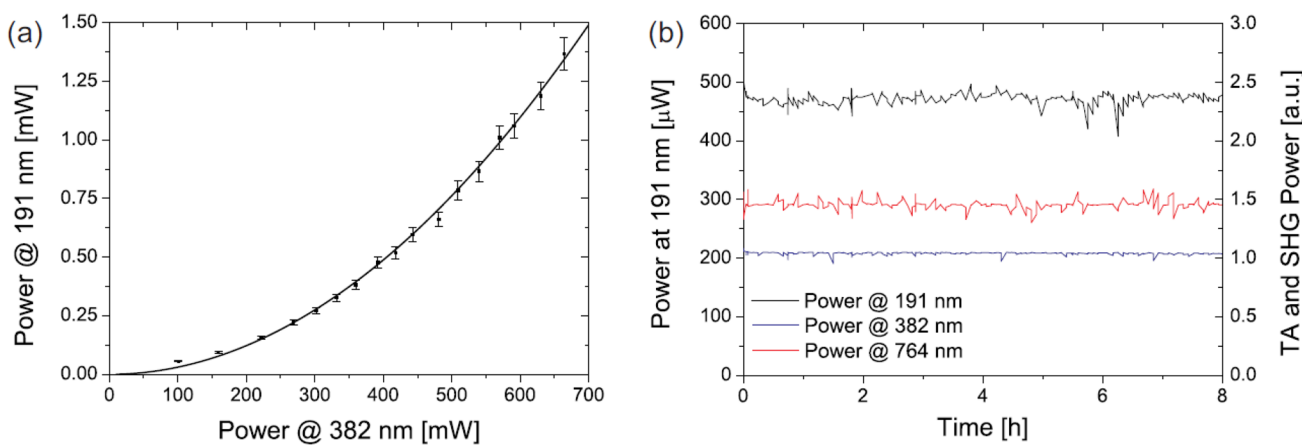


**Fig. 20** **a** Dependence of the DUV power at 191 nm on the pump power. The solid line represents a simulation of the generated DUV power. **b** Long-term measurement of the TA, SHG, and DUV power

over a interval of 8 h. None of the signals shows a degradation over time. ([Reprinted/Adapted] with permission from Scholz et al. [55] © The Optical Society)

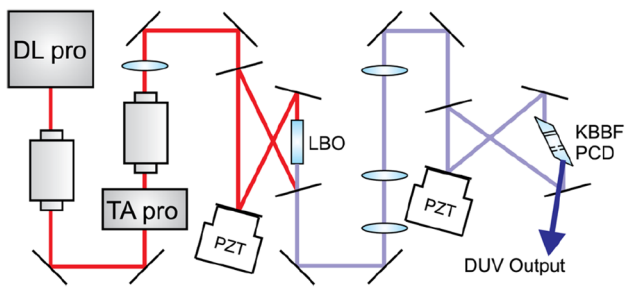


**Fig. 21** Experimental setup of the described deep-ultraviolet laser source. (Scholz et al. [56], licensed under a Creative Commons Attribution (CC BY) license)

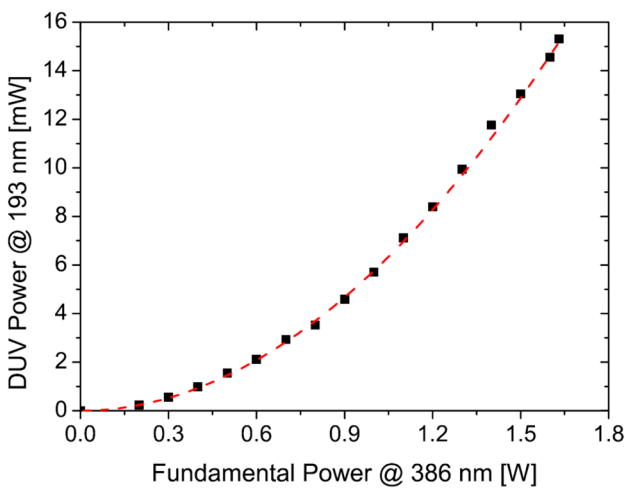


**Fig. 22** Dependence of the deep-ultraviolet output power on the fundamental power at 386 nm. (Scholz et al. [56], licensed under a Creative Commons Attribution (CC BY) license)

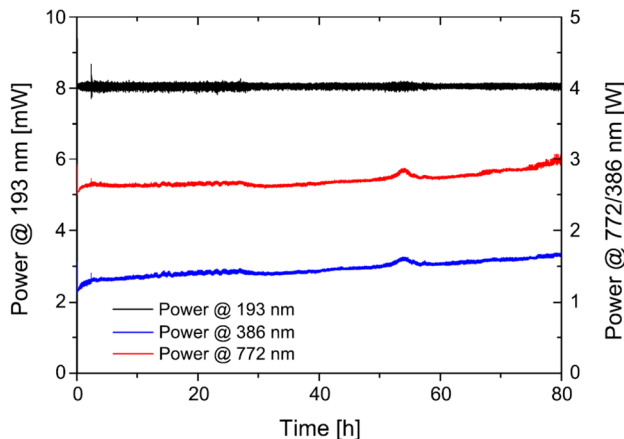


**Fig. 23** Long-term measurement of the deep-ultraviolet output power, the second harmonic output at 386 nm, and the tapered-amplifier pump power at 772 nm over a time interval of 80 h. (Scholz et al. [56], licensed under a Creative Commons Attribution (CC BY) license)

super-high-energy and momentum resolutions, VUV laser-based spin- and angle-resolved photoemission spectroscopy (SARPES), VUV laser-based angle-resolved time-of-flight photoemission spectroscopy (TOF-ARPES) and so on. These ARPES systems have made important contributions to the study of high-temperature superconductors and topological materials [58–60].

For the VUV laser ARPES system, the generation of 6.994 eV laser light and the advent of new electron energy analyzers that can work properly at a low electron kinetic energy have made it possible for the ARPES system to exhibit superior performance [57]. Taking advantage of its super-high-energy resolution and high data statistic, ARPES becomes a powerful tool to probe the many-body

effects in materials [61]. In the high-temperature superconductors fields, many-body effects show up as electron-boson coupling qualitatively in the electron self-energy and are quantitatively expressed by the electron coupling function, the Eliashberg function. Due to the super-high-energy and momentum resolutions of the VUV laser ARPES, several new coupling modes have been identified in  $\text{Bi}_2\text{Sr}_2\text{CaCu}_2\text{O}_{8+\delta}$  (Bi2212) [62], and the momentum dependences of the coupling modes are revealed [63]. However, just knowing the existence of mode-coupling is not enough to understand the many-body effects comprehensively and it is necessary to extract the detailed coupling function—the Eliashberg function. No attempts have been successful for this extraction until VUV laser-based ARPES are developed. Such extraction is successfully applied in Bi2212 and the related results are shown in Fig. 24 [64, 65]. Based on the high quality of the ARPES data taken below and above the superconducting transition temperature, the normal Eliashberg function and the pairing Eliashberg function are extracted. This is the first time that the pairing Eliashberg functions are extracted from ARPES measurements. They provide critical information for understanding the high-temperature superconductivity mechanism.

For the VUV laser-based SARPES, Mott detectors are used to resolve the spin structure, which have been proven to be very stable and reliable. The high photon flux of the VUV laser can compensate the low efficiency of the Mott spin detector while not losing the overall high-energy resolution of the system. The best energy resolution achieved in the spin mode is  $\sim 2.5$  meV [66] which is much better than

the usual 50–100 meV energy resolution of synchrotron light source-based spin-ARPES measurements [67, 68].

For the VUV laser-based ARTOF-ARPES system, it is equipped with the latest generation of angle-resolved time-of-flight (ARToF) electron energy analyzer which can cover the two-dimensional angle space simultaneously [58]. It transforms ARPES measurement from one-line momentum cut to an area momentum coverage and increases the angle acquisition efficiency significantly. The low photoelectron energy excited by the VUV laser also can make it possible for the TOF-ARPES system to achieve high-energy resolution better than 1 meV. It plays important roles in detecting fine electronic structure on the small-sized samples.

The emergence of the VUV light source has endowed ARPES technique with unique and superior performances. In studying quantum materials like high-temperature superconductors and topological materials, a series of VUV laser-based ARPES systems have demonstrated their great power. They will also make greater progress with the further development of the VUV laser and the electron energy analyzer in future.

## 7 Conclusion

It has been 25 years since KBBF was first proved to be a deep-UV NLO crystal in 1996. With the help of PCDs, KBBF crystal becomes the only practical deep-UV NLO crystal at present. The success of KBBF crystal growth was based on the “localized spontaneous nucleation method” in

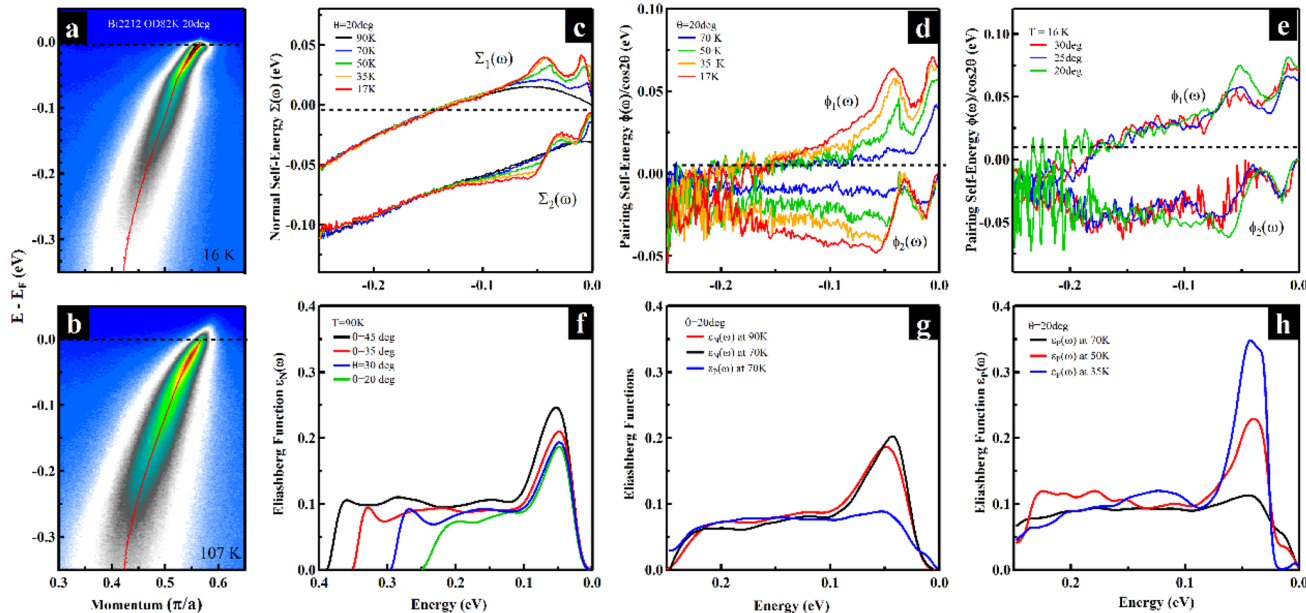


**Fig. 24** Extraction of Eliashberg functions from VUV laser-based ARPES on Bi2212. Extracted normal Eliashberg function and pairing Eliashberg function for Bi2212 are shown

the past decade. So far, several deep-UV lasers based on KBBF-PCDs have been successfully applied in the advanced scientific instruments, especially in ARPES.

A generation of materials, a generation of technology. In future, the development of all-solid-state deep-UV lasers will still depend on deep-UV NLO crystals. Some potential deep-UV NLO crystals (or compounds), such as  $\gamma$ -Be<sub>2</sub>BO<sub>3</sub>F and some fluorooxoborates, have emerged. However, they are still far from useful crystals. KBBF-PCDs are still going to play a crucial role in all-solid-state deep-UV lasers. The next goal is to fabricate prism-free devices, which need KBBF crystals with sufficient thickness (along the Z-axis). It requires the development of new growth methods and relevant cutting technology to solve the crystal cleavage problem. However, the strong-layered behavior of KBBF is an intrinsic obstacle, which may not be overcome eventually. An alternative breakthrough would come from the discovery and development of new deep-UV NLO crystals. With these and future progresses, all-solid-state deep-UV lasers will open up more application fields and play a greater role in the frontiers of science and technology.

**Acknowledgements** We acknowledge collaborations with Prof. Zuyan Xu's group in developing deep-UV lasers. This work was supported by the National Natural Science Foundation of China (51890864), the National Natural Science Foundation of China (11888101, 11922414), the Strategic Priority Research Program (B) of the Chinese Academy of Sciences (Grant No. XDB25000000). We would like to commemorate Professor Chen Chuangtian with this article.

## References

1. H.W. Xuan, C. Qu, Z.G. Zhao, S.J. Ito, Y. Kobayashi, Opt. Express **25**(23), 29172 (2017)
2. T. Kiss, T. Shimojima, K. Ishizaka, A. Chainani, T. Togashi, T. Kanai, X.Y. Wang, C.T. Chen, S. Watanabe, S. Shin, Rev. Sci. Instrum. **79**, 023106 (2008)
3. C.T. Chen, G.L. Wang, X.Y. Wang, Z.Y. Xu, Appl. Phys. B **97**, 9–25 (2009)
4. C.T. Chen, B.C. Wu, A.D. Jiang, G. You, Sci. Sin. B **28**, 235 (1985)
5. C.T. Chen, Act. Phys. Sin. **25**(2), 146–161 (1976)
6. C.T. Chen, Act. Phys. Sin. **26**(2), 124–132 (1977)
7. C.T. Chen, Act. Phys. Sin. **26**(6), 486–499 (1977)
8. C.T. Chen, Act. Phys. Sin. **27**(1), 42–46 (1978)
9. C.T. Chen, *Development of New NLO Crystals in the Borate Series. Laser Science and Technology, an International Handbook* (Plenum Press, Cham, 1993)
10. C.T. Chen, Y.C. Wu, A.D. Jiang, B.C. Wu, G.M. You, R.K. Li, S.J. Lin, J. Opt. Soc. Am. B **6**(4), 616–621 (1989)
11. L.F. Mei, C. He, C.T. Chen, J. Cryst. Growth **132**, 609 (1993)
12. C.T. Chen, S.Y. Luo, X.Y. Wang, G.L. Wang, X.H. Wen, H.X. Wu, X. Zhang, Z.Y. Xu, J. Opt. Soc. Am. B **26**(8), 1519–1525 (2009)
13. D.N. Nikogosyan, *Nonlinear Optical Crystals: A Complete Survey* (Springer, Berlin, 2005)
14. C.T. Chen, Z.Y. Xu, D.Q. Deng, J.Y. Zhang, G.K.L. Wong, B.C. Wu, N. Ye, D.Y. Tang, Appl. Phys. Lett. **68**(21), 2930–2932 (1996)
15. D. Cyranoski, Nature **457**, 953–955 (2009)
16. C.T. Chen, Y. Wang, B.C. Wu, K. Wu, W. Zeng, L.H. Yu, Nature **373**, 322–324 (1995)
17. H. Qi, C.T. Chen, Chem. Lett. **30**(4), 352–353 (2001)
18. H.W. Huang, J.Y. Yao, Z.S. Lin, X.Y. Wang, R. He, W.J. Yao, N.X. Zhai, C.T. Chen, Chem. Mater. **23**, 5457–5463 (2011)
19. H.W. Huang, J.Y. Yao, Z.S. Lin, X.Y. Wang, R. He, W.J. Yao, N.X. Zhai, C.T. Chen, Angew. Chem. **50**, 9141–9144 (2011)
20. S.C. Wang, N. Ye, W. Li, D. Zhao, J. Am. Chem. Soc. **132**, 8779–8786 (2010)
21. W.J. Yao, R. He, X.Y. Wang, Z.S. Lin, C.T. Chen, Adv. Opt. Mater. **2**, 411–417 (2014)
22. G. Cakmak, J. Nuss, M. Jansen, Z. Anorg. Allg. Chem. **635**, 631–636 (2009)
23. T. Pilz, H. Nuss, M. Jansen, J. Solid State Chem. **186**, 104–108 (2012)
24. T. Pilz, M. Jansen, Z. Anorg. Allg. Chem. **637**(14–15), 2148–2152 (2011)
25. G.Q. Shi, Y. Wang, F.F. Zhang, B.B. Zhang, Z.H. Yang, X.L. Hou, S.L. Pan, K.R. Poepelmeier, J. Am. Chem. Soc. **139**(31), 10645–10648 (2017)
26. X.F. Wang, Y. Wang, B.B. Zhang, F.F. Zhang, Z.H. Yang, S.L. Pan, Angew. Chem. Int. Ed. **56**, 14119–14123 (2017)
27. Y. Wang, B. Zhang, Z. Yang, S. Pan, Angew. Chem. Int. Ed. **57**, 2150–2154 (2018)
28. Z.Z. Zhang, Y. Wang, B.B. Zhang, Z.Y. Yang, S.L. Pan, Angew. Chem. Int. Ed. **57**, 6577–6581 (2018)
29. Z.Z. Zhang, Y. Wang, B.B. Zhang, Z.H. Yang, S.L. Pan, Inorg. Chem. **57**, 4820–4823 (2018)
30. M. Mutailipu, M. Zhang, B. Zhang, L. Wang, Z. Yang, X. Zhou, S. Pan, Opt. Mater. Angew. Chem. Int. Ed. **57**, 6095–6099 (2018)
31. M. Luo, F. Liang, Y. Song, D. Zhao, F. Xu, N. Ye, Z. Lin, J. Am. Chem. Soc. **140**, 3884–3887 (2018)
32. G. Peng, N. Ye, Z.L. Lin, L. Kang, S.L. Pan, M. Zhang, C.S. Lin, X.F. Long, M. Luo, Y. Chen, Y.H. Tang, F. Xu, T. Yan, Angew. Chem. Int. Ed. **57**, 8968–8972 (2018)
33. S. Guo, L.J. Liu, M.J. Xia, L. Kang, Q. Huang, C. Li, X.Y. Wang, Z.S. Lin, C.T. Chen, Inorg. Chem. **55**, 6586–6591 (2016)
34. L.R. Batsanova, V.A. Egorov, Dokl. Akad. Nauk SSSR **178**, 1317 (1968)
35. M. Miriding, M. Zhang, Z.H. Yang, S.L. Pan, Acc. Chem. Res. **52**, 791–801 (2019)
36. X.Y. Wang, X. Yan, S.Y. Luo, C.T. Chen, J. Cryst. Growth **318**, 610–612 (2011)
37. N. Ye, D.Y. Tang, J. Cryst. Growth **293**, 233–235 (2006)
38. C.D. McMillen, J.W. Kolis, J. Cryst. Growth **310**, 2033–2038 (2008)
39. L.J. Liu, T. Xu, X.L. Wang, C.T. Chen, J. Cryst. Growth **401**, 824–827 (2014)
40. H.T. Zhou, X.L. He, W.N. Zhou, Z.G. Hu, C.L. Zhang, H.D. Huo, J.L. Wang, S.J. Qin, Y.B. Zuo, F.H. Lu, J. Cryst. Growth **318**, 613–617 (2011)
41. J.Q. Yu, L.J. Liu, S.F. Jin, H.T. Zhou, X.L. He, C.L. Zhang, W.N. Zhou, X.Y. Wang, X.L. Chen, C.T. Chen, J. Solid State Chem. **184**, 2790–2793 (2011)
42. Y.H. Sang, D.H. Yu, M. Avdeev, R. Piltz, N. Sharma, N. Ye, H. Liu, J.Y. Wang, CrystEngComm **14**, 6079–6084 (2012)
43. T. Xu, L.J. Liu, X.Y. Wang, C.T. Chen, Dalton. Trans. **43**, 16411–16415 (2014)
44. C.T. Chen, G.L. Wang, X.Y. Wang, Y. Zhu, Z.Y. Xu, T. Kanai, IEEE J. Quantum Electron. **44**(7), 617–621 (2008)
45. T. Nakazato, I. Ito, Y. Kobayashi, X.Y. Wang, C.T. Chen, S. Watanabe, Opt. Express **24**, 17149–17158 (2016)

46. R.K. Li, L.R. Wang, X.Y. Wang, G.L. Wang, C.T. Chen, *App. Opt.* **55**(36), 10423–10426 (2016)
47. C.T. Chen, J.H. Lu, G.L. Wang, Z.Y. Xu, J.Y. Wang, C.Q. Zhang, Y.G. Liu, *Chin. Phys. Lett.* **18**(8), 1081 (2001)
48. T. Togashi, T. Kanai, T. Sekikawa, S. Watanabe, C.T. Chen, C.Q. Zhang, Z.Y. Xu, J.Y. Wang, *Opt. Lett.* **28**(4), 254 (2003)
49. C.T. Chen, Y. Zhu, F.D. Fan, X.Y. Wang, R.K. Li, Optical coupling device having KBBF group crystal coupled with prisms and method for manufacturing same, US patent, US 8,773,750 B2 (2014)
50. B. Xu, L.J. Liu, X.Y. Wang, C.T. Chen, X. Zhang, S.J. Lin, *Appl. Phys. B* **121**, 489–494 (2015)
51. Y. Nomura, Y. Ito, A. Ozawa, X. Wang, C. Chen, S. Shin, S. Watanabe, Y. Kobayashi, *Opt. Lett.* **36**(10), 1758–1760 (2011)
52. S.B. Dai, N. Zong, F. Yang, S.J. Zhang, Z.M. Wang, F.F. Zhang, W. Tu, L.Q. Shang, L.J. Liu, X.Y. Wang, J.Y. Zhang, D.F. Cui, Q.J. Peng, R.K. Li, C.T. Chen, Z.Y. Xu, *Opt. Lett.* **40**(14), 3268–3271 (2015)
53. J.J. Li, F.F. Zhang, Z.M. Wang, Y.C. Xu, X.C. Liu, N. Zong, S.J. Zhang, F.L. Xu, F. Yang, L. Yuan, Y. Kou, Y. Bo, D.F. Cui, Q.J. Peng, X.Y. Wang, L.J. Liu, C.T. Chen, Z.Y. Xu, *Opt. Lett.* **43**(11), 2563–2566 (2018)
54. S.B. Dai, M. Chen, S.J. Zhang, Z.M. Wang, F.F. Zhang, F. Yang, Z.C. Wang, N. Zong, L.J. Liu, X.Y. Wang, J.Y. Zhang, Y. Bo, D.F. Cui, Q.J. Peng, R.K. Li, C.T. Chen, Z.Y. Xu, *Laser Phys. Lett.* **13**, 035401 (2016)
55. M. Scholz, D. Opalevs, P. Leisching, W. Kaenders, G.L. Wang, X.Y. Wang, R.K. Li, C.T. Chen, *Opt. Express* **20**(17), 18659–18664 (2012)
56. M. Scholz, D. Opalevs, P. Leisching, W. Kaenders, G.L. Wang, X.Y. Wang, R.K. Li, C.T. Chen, *Appl. Phys. Lett.* **103**, 051114 (2013)
57. G.D. Liu, G.L. Wang, Y. Zhu, H.B. Zhang, G.C. Zhang, X.Y. Wang, Y. Zhou, W.T. Zhang, H.Y. Liu, L. Zhao, J.Q. Meng, X.L. Dong, C.T. Chen, Z.Y. Xu, X.J. Zhou, *Rev. Sci. Instrum.* **79**, 023105 (2008)
58. X.J. Zhou, S.L. He, G.D. Liu, L. Zhao, L. Yu, W.T. Zhang, *Rep. Prog. Phys.* **81**, 062101 (2018)
59. L. Zhao, G.D. Liu, X.J. Zhou, *Acta Phys. Sin.* **67**(20), 207413 (2018)
60. L. Zhao, G.D. Liu, X.J. Zhou, *Acta Phys. Sin.* **70**, 017406 (2021)
61. X. J. Zhou, T. Cuk, T. Devereaux, N. Nagaosa, Z.X. Shen, in *Angle-Resolved Photoemission Spectroscopy on Electronic Structure and Electron-Phonon Coupling in Cuprate Superconductors, Handbook of High Temperature Superconductivity: Theory and Experiment*, ed. by J. R. Schrieffer (Springer, New York, 2007)
62. W.T. Zhang, G.D. Liu, L. Zhao, H.Y. Liu, J.Q. Meng, X.L. Dong, W. Lu, J.S. Wen, Z.J. Xu, G.D. Gu, T. Sasagawa, G.L. Wang, Y. Zhu, H.B. Zhang, Y. Zhou, X.Y. Wang, Z.X. Zhao, C.T. Chen, Z.Y. Xu, X.J. Zhou, *Phys. Rev. Lett.* **100**, 107002 (2008)
63. J.F. He, W.T. Zhang, J.M. Bok, D.X. Mou, L. Zhao, Y.Y. Peng, S.L. He, G.D. Liu, X.L. Dong, J. Zhang, J.S. Wen, Z.J. Xu, G.D. Gu, X.Y. Wang, Q.J. Peng, Z.M. Wang, S.J. Zhang, F. Yang, C.T. Chen, Z.Y. Xu, H.Y. Choi, C.M. Varma, X.J. Zhou, *Phys. Rev. Lett.* **111**, 107005 (2013)
64. J.M. Bok, J.H. Yun, H.Y. Choi, W.T. Zhang, X.J. Zhou, C.M. Varma, *Phys. Rev. B* **81**, 174516 (2010)
65. J.M. Bok, J.J. Bae, H.Y. Choi, C.M. Varma, W.T. Zhang, J.F. He, Y.X. Zhang, L. Yu, X.J. Zhang, *Sci. Adv.* **2**, e1501329 (2016)
66. Z.J. Xie, S.L. He, C.Y. Chen, Y. Feng, H.M. Yi, A.J. Liang, L. Zhao, D.X. Mou, J.F. He, Y.Y. Peng, X. Liu, Y. Liu, G.D. Liu, X.L. Dong, L. Yu, J. Zhang, S.J. Zhang, Z.M. Wang, F.F. Zhang, F. Yang, Q.J. Peng, X.Y. Wang, C.T. Chen, Z.Y. Xu, X.J. Zhou, *Nat. Commun.* **5**, 3382 (2014)
67. S. Qiao, A. Kimura, A. Harasawa, M. Sawada, J.G. Chung, A. Kakizaki, *Rev. Sci. Instrum.* **68**, 4390–4395 (1997)
68. M. Hoesch, T. Greber, V.N. Petrov, M. Muntwiler, M. Hengsberger, W. Auwarter, J. Osterwalder, *J. Electron Spectrosc. Relat. Phenom.* **124**, 263–279 (2002)

**Publisher's Note** Springer Nature remains neutral with regard to jurisdictional claims in published maps and institutional affiliations.

## Terms and Conditions

Springer Nature journal content, brought to you courtesy of Springer Nature Customer Service Center GmbH (“Springer Nature”). Springer Nature supports a reasonable amount of sharing of research papers by authors, subscribers and authorised users (“Users”), for small-scale personal, non-commercial use provided that all copyright, trade and service marks and other proprietary notices are maintained. By accessing, sharing, receiving or otherwise using the Springer Nature journal content you agree to these terms of use (“Terms”). For these purposes, Springer Nature considers academic use (by researchers and students) to be non-commercial.

These Terms are supplementary and will apply in addition to any applicable website terms and conditions, a relevant site licence or a personal subscription. These Terms will prevail over any conflict or ambiguity with regards to the relevant terms, a site licence or a personal subscription (to the extent of the conflict or ambiguity only). For Creative Commons-licensed articles, the terms of the Creative Commons license used will apply.

We collect and use personal data to provide access to the Springer Nature journal content. We may also use these personal data internally within ResearchGate and Springer Nature and as agreed share it, in an anonymised way, for purposes of tracking, analysis and reporting. We will not otherwise disclose your personal data outside the ResearchGate or the Springer Nature group of companies unless we have your permission as detailed in the Privacy Policy.

While Users may use the Springer Nature journal content for small scale, personal non-commercial use, it is important to note that Users may not:

1. use such content for the purpose of providing other users with access on a regular or large scale basis or as a means to circumvent access control;
2. use such content where to do so would be considered a criminal or statutory offence in any jurisdiction, or gives rise to civil liability, or is otherwise unlawful;
3. falsely or misleadingly imply or suggest endorsement, approval , sponsorship, or association unless explicitly agreed to by Springer Nature in writing;
4. use bots or other automated methods to access the content or redirect messages
5. override any security feature or exclusionary protocol; or
6. share the content in order to create substitute for Springer Nature products or services or a systematic database of Springer Nature journal content.

In line with the restriction against commercial use, Springer Nature does not permit the creation of a product or service that creates revenue, royalties, rent or income from our content or its inclusion as part of a paid for service or for other commercial gain. Springer Nature journal content cannot be used for inter-library loans and librarians may not upload Springer Nature journal content on a large scale into their, or any other, institutional repository.

These terms of use are reviewed regularly and may be amended at any time. Springer Nature is not obligated to publish any information or content on this website and may remove it or features or functionality at our sole discretion, at any time with or without notice. Springer Nature may revoke this licence to you at any time and remove access to any copies of the Springer Nature journal content which have been saved.

To the fullest extent permitted by law, Springer Nature makes no warranties, representations or guarantees to Users, either express or implied with respect to the Springer nature journal content and all parties disclaim and waive any implied warranties or warranties imposed by law, including merchantability or fitness for any particular purpose.

Please note that these rights do not automatically extend to content, data or other material published by Springer Nature that may be licensed from third parties.

If you would like to use or distribute our Springer Nature journal content to a wider audience or on a regular basis or in any other manner not expressly permitted by these Terms, please contact Springer Nature at

[onlineservice@springernature.com](mailto:onlineservice@springernature.com)